ELSEVIER

Kinetics and visualization of soot oxidation using transmission electron microscopy

Heejung Jung,[a] David B. Kittelson,[a] and Michael R. Zachariah [a,b,*]

[a] *Department of Mechanical Engineering, University of Minnesota, 111 Church Street SE, Minneapolis, MN 55455, USA*
[b] *Department of Chemistry, University of Minnesota, 111 Church Street SE, Minneapolis, MN 55455, USA*

Abstract

Visualization of the oxidation of individual soot particles using transmission electron microscopy (TEM) was performed and quantitative oxidation rates were determined. Soot particles were sampled from an ethylene diffusion flame burner and collected on a TEM grid. Individual particles were then tracked by creating maps of TEM images at different magnifications, and images were compared before and after the oxidation process in a separate furnace at low temperatures (< 800 K). Mono-area soot particles were sampled on TEM grids using a differential mobility analyzer (DMA) and a low-pressure impactor. It was found that the mobility equivalent diameter determined by the DMA is equivalent to the projected area equivalent diameter determined by the TEM for particles below 150 nm. Groups of mono-area particles were visualized before and after the oxidation process and oxidation rates were determined from the change in projected area equivalent diameter by image-processing a series of TEM images. For these low temperatures (< 800 K), an activation energy of 148 kJ/mol was found for the oxidation of soot particles. The overall oxidation rate was found to be significantly higher than in prior studies, and some possible reasons for the discrepancy discussed.
© 2003 Published by Elsevier Inc. on behalf of The Combustion Institute.

Keywords: Soot; Oxidation; Kinetics; Visualization; TEM; Soot combustion

1. Introduction

With the great emphasis being placed on high-efficiency power generation, diesel engines are increasingly being looked upon as the technology of choice. In turn this has intensified the interest in methods and technologies to reduce soot emissions. It is unlikely that it will be possible to meet future particle emission standards without the use of aftertreatment devices like the diesel particulate filter (DPF). Under typical operating conditions, diesel exhaust temperatures may be quite low, below about 300 °C. The performance of DPFs is highly dependent on the rate at which soot oxidizes and requires a more detailed understanding than is currently available, particularly at low temperatures. Earlier works on the measurement of low-temperature oxidation included thermo gravimetric analysis (TGA) [1,2] or flow reactors with stationary soot beds [3,4]. While TGA is convenient, it is known to be plagued by heat and mass transfer effects, which make the data interpretation and quantification of the intrinsic kinetics difficult. In a recent study we have shown that the reactivity of nanoparticles can be underestimated by as much as 3 orders of magnitude using TGA [5]. Furthermore these studies also showed that the reaction constants extracted by these means were very sensitive to the sample mass used in the TGA. The use of flow reactors with fixed beds also requires the use of bulk soot samples and is therefore presumably also corrupted by similar heat and mass transfer limitations.

---

* Corresponding author.
  E-mail address: mrz@me.umn.edu (M.R. Zachariah).

Fundamentally therefore it would be preferable to assess the reactivity of a single soot particle to extract the nascent intrinsic chemical kinetic rates. Ishiguro et al. [6] investigated the morphology change of soot during oxidation using an electron microscope and FTIR spectroscopy. Their investigation focused on microstructural analysis, such as the behavior of crystallites in soot during oxidation. However, they did not use this approach to quantify the oxidation rate. Tanaka [7] also visualized the oxidation of soot particles using transmission electron microscopy (TEM). He collected diesel soot particles on a thin Al_2O_3 plate and tracked their change in size using TEM images. He chose a single agglomerate about 0.5 μm in size and observed that each of the primary particles gets smaller as it is oxidized.

The work presented in this paper takes the work of Tanaka [7] a step further. Soot particles extracted from a diffusion flame were size segregated by differential mobility and deposited on TEM grids. A group of approximately 100 particles was tracked to examine the change in morphology and size as a function of oxidation time and temperature. To extract quantitative rates the images were processed in terms of projected area equivalent diameter. The results of this paper are the development of an experimental protocol to measure the oxidation rate of soot particles at low temperatures (< 800 K) using TEM image analysis.

2. Experimental

2.1. Soot source, size selection, and sampling

Figures 1a and 1b show diagrams of the experimental setups used in the current study. Soot particles were generated using a Santoro-type diffusion flame burner [8], using ethylene as the fuel. A 10-in. high glass shroud is placed on the outer tube to prevent the flame from being disturbed by outside air currents. The flame was maintained at 50 mm high at an ethylene fuel flow rate of 85 $cm^3 min^{-1}$.

The sampling probe used in this study is similar to one described in our prior work [9]. Soot particles were extracted at the tip of the flame through a 1-mm orifice in the bottom of an 11-mm diameter sampling probe and diluted by a 20 L min^{-1} flow of filtered clean dry air. More detailed information on this burner and the sampling probe has been previously described [9]. Because soot particles generated in the flame are highly charged with many more multiply charged particles than an equilibrium charge distribution at room temperature, the extracted soot particles were sent through a bipolar diffusion charger

(neutralizer) to establish a known charge distribution. Particles were then passed through a differential mobility analyzer (DMA). The DMA selects mono-area particles based on electrical mobility, which is related to the drag and charge on a particle rather than on absolute particle size. This means larger particles with multiple charges will pass through at the same voltage setting as the singly charged particles of the size of interest. For the particle sizes used in the current study, the majority of charged particles in an equilibrium charge distribution will carry a single charge and the minority of multiply charged particles will also pass through the DMA. These mono-area particles were subjected to three possible fates as illustrated in Figs. 1a–1c. In experiments shown in Figs. 1a and 1b, we used the lowest stage of a low-pressure impactor [10], after removal of the impaction plates in the higher states, as an efficient means to deposit particles on a TEM grid. The initial size distribution of particles collected on the TEM grid was obtained using TEM image analysis. Next, the particles on the TEM grid were oxidized in a furnace and subsequently underwent TEM analysis to observe the change in size. Figure 1b shows an experimental system in which particles were oxidized in free flight in a heated flow tube of known residence time and temperature profile. The particles were collected in the same manner as in Fig. 1a and analyzed using TEM analysis. Finally, Fig. 1c shows a tandem-DMA experiment we have previously reported on, in which the change in size after the flow-tube oxidation was measured with a second differential mobility analyzer [9]. The tandem-DMA system shown in Fig. 1c is used for high-temperature oxidation studies, but is not amenable for studying slow reactions due to the long residence times required. On the other hand the system depicted in Fig. 1a, in which the sample is prepared and then placed with the grid in an oven, cannot be used at high temperatures at which the chemistry is fast. In order to provide a check of consistency between these two approaches, we used the configuration depicted in Fig. 1b, in which, subsequent to oxidation and deposition, we conducted the same image analysis procedure as used in experimental system 1a.

2.2. Soot oxidation

Following the deposition of the size-selected soot on the TEM grids, a portion which has sufficient particles to provide statistically meaningful data was selected. A series of TEM images (Model JEOL 1210) was taken using a digital CCD camera from low to high magnification as shown in Fig. 2. This enabled us to create maps on which the same particles could be located later on. We found that TEM grids with
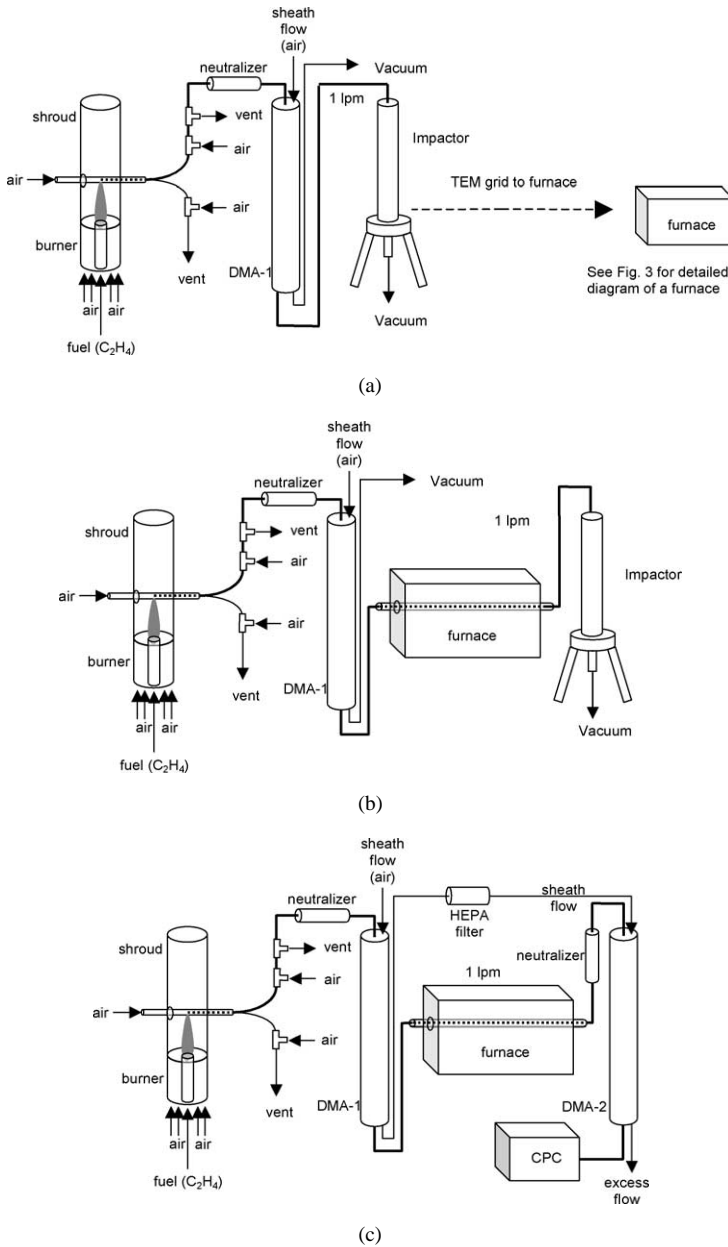
Fig. 1. Schematic diagram of the experimental setups. (a) Setup for TEM sampling. (b) Setup to compare the current study with the results of Higgins et al. [9,18]. (c) The setup of Higgins et al. [9]. The setup used in Higgins et al. [18] is the same except the particle source is a diesel engine.

holey or lacy film provided easily identifiable geo-metric features enabling one to relocate particular particles. Because the grids were to be removed and subjected to an elevated-temperature oxidizing envi-ronment (air) we could not use the standard carbon-coated grids, but rather employed nickel mesh with a holey silicon oxide film.

Once a map of the grid was made the grid could then be removed and inserted into a furnace for a

specified time and temperature as shown in Fig. 3. The mechanics of the experiment shown in Fig. 3 involved loading the TEM grid (3 mm in diameter) into a very low heat capacity stainless steel foil cru-cible (thickness of 25 μm and $10 \times 10 \times 3$ mm). The tube furnace, which has a 300-mm heating zone, con-tained a 25-mm-diameter alumina outer tube and a 15-mm-diameter inner quartz tube. The purpose of the second quartz tube was simply for convenience
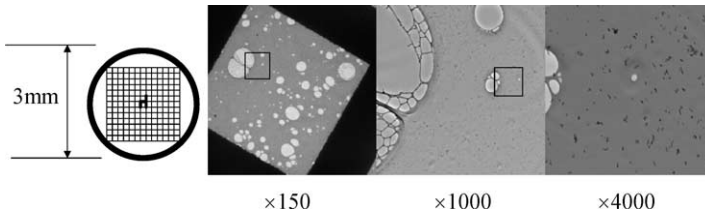
Fig. 2. Maps of TEM images to track a field of view.
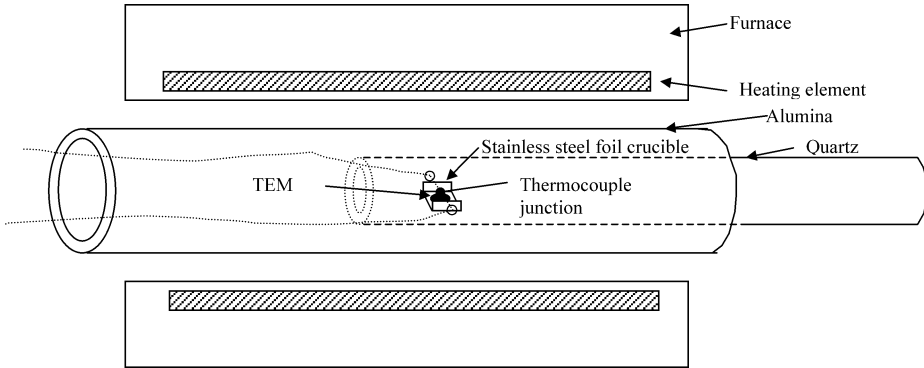
Fig. 3. Schematic diagram of a furnace.

of allowing the sample to be rapidly inserted and removed. To minimize transient temperature effects, the unloaded crucible was first thermalized in the flow oven for 1 h to reach steady-state temperature conditions, after which the quartz tube with the crucible was partially removed to load the TEM grid containing the particles. Despite the care taken to thermalize the system and the use of low-heat-capacity structures, a transient temperature profile was still evident as shown in Fig. 4. The temperature profile shown here was measured with a 0.05-mm-diameter type K fine wire thermocouple. While this measurement was made without the crucible, it should be a fairly accurate representation of the time–temperature history experienced by the particles. We have estimated the temperature uncertainty to be less than ± 2 K and it is described in Appendix A.

Soot particles on the TEM grid were oxidized in heated air for a given time and temperature. Analysis of the oxidation-exposed grid used the same field of view as was used prior to oxidation using the procedure illustrated in Fig. 2.

3. Results and discussion

3.1. Visualization of soot oxidation

3.1.1. Tracking individual particles

Figure 5 shows examples of individual particles during oxidation at different cumulative oxidation
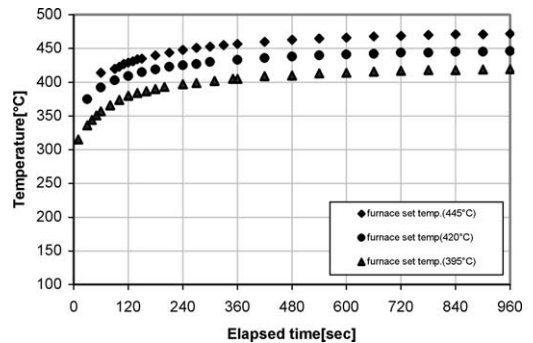
Fig. 4. Temperature profile of a furnace, at the place where the oxidation of soot particles occurs, as a function of elapsed time.

times at 450 °C. Initial images of particles (a) and (e) were taken and those particles were tracked separately. The soot aggregates are composed of primary particles in the 20–30 nm size range. Clearly the primary particles are shown shrinking during this process, but we also observe some changes in the aggregate morphology. The latter observation presumably has to do with how the particles find themselves anchored to the grid, and one might expect differences from what might occur in the gas phase. Most of the primary particles were observed to shrink evenly during oxidation. For these particular images an arm of the aggregate seemed to move during oxidation (Figs. 5a–5d), whereas the particle in Figs. 5e–5h
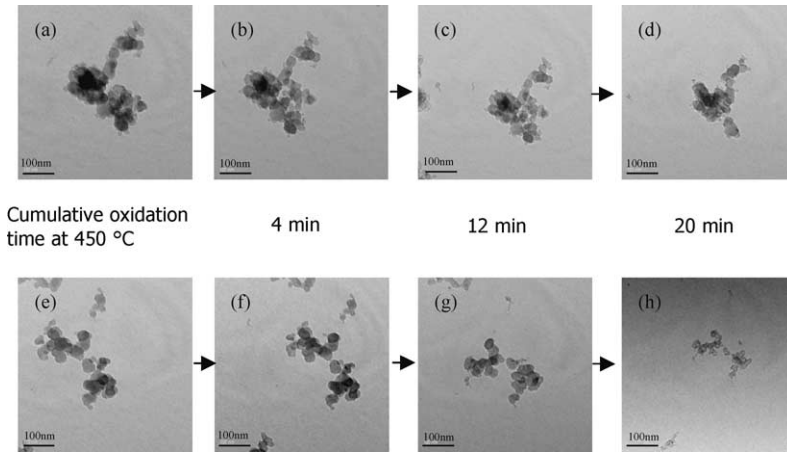
Fig. 5. TEM images during oxidation for individual particles.

shrank in size without significant changes in shape. Our more gradual evolving particle shape and size are in contrast to the observations of Heckman [11]. He employed high-temperature heat treatment (partial graphitization in an inert atmosphere) before carrying out an oxidation experiment. His work found very little shrinkage, but rather an internal hollowing out of the particles. He speculated that a more ordered graphitic layer structure, at the surface of the particles, was stable against oxidation, and Gilot et al. [12] also reported internal oxidation of carbon black spherules after 60% burn-off at low temperature. We observed no selective hollowing of soot particles in this study, which we believe is related to the absence of a pregraphitization process [13].

To quantify the results of the oxidation we used a public domain image program (NIH Image [14]) to obtain the projected particle area. Using the software, for example, on the images in Fig. 5, we can determine that particle (e) has a projected area equivalent diameter of 178 nm and that after oxidation for 20 min the resulting particle (h) has shrunk to a projected area equivalent diameter of 108 nm. Our goal is to relate the projected area change to the surface-specific reaction rate for soot oxidation. Since individual particles can undergo different projected area reduction rates due to the facts that a portion of a particle can disappear during oxidation and the oxidation rate can be different due to differences in chemical composition for individual particles, we tracked a group of particles rather than individual particles to quantify the oxidation rate.

3.1.2. Tracking a group of particles

A field of view containing about 100 particles was chosen for tracking during oxidation. In order to observe such a large number of particles in a single im-

age the magnification used ($\times4000$–$\times5000$) is about six times lower than that used for tracking individual particles and is shown in Fig. 6a. Figure 6b shows the image after oxidation in a furnace for 4 min at a set temperature of 450 °C. Qualitatively we see that particles are clearly shrinking, but that some particles are seen to be oxidizing faster than others and in some cases disappear entirely. These differences in oxidation rate would seem to indicate that even though all particles were sampled from a single location and size segregated with a DMA, they may not be chemically the same. Particles that disappeared were excluded manually during image analysis so that the exact same group of particles could be tracked.

Figure 7 shows the same area after image processing with the image program (NIH Image [14]). The image shown is after digital filtering to remove the background and conversion to a binary image. Pixels that could not be removed, but that obviously were not particles, were erased manually. Next, the image program (NIH Image [14]) obtained the projected area for each particle, from which we could determine the projected area equivalent diameter (the diameter of a sphere that has the same projected area as that of the particle of interest). The number of particles at a given constant $\Delta \log(d_p)$ bin was counted using a simple sorting program to draw a number size distribution as a function of projected area equivalent diameter.

Figure 8 shows the resulting size distributions for particles in Figs. 6 and 7 using the data analysis procedure described. Clearly the size distribution has both shifted to lower sizes and broadened. The results are qualitatively remarkably consistent with our prior tandem-DMA oxidation studies in which we observed changes in size resulting in oxidation using a second DMA to observe size changes [9].
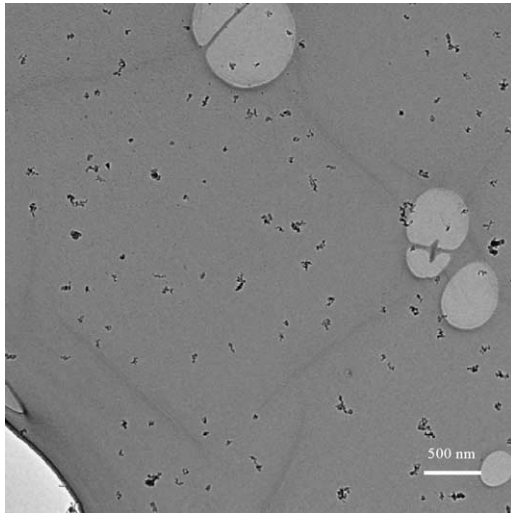
(a)
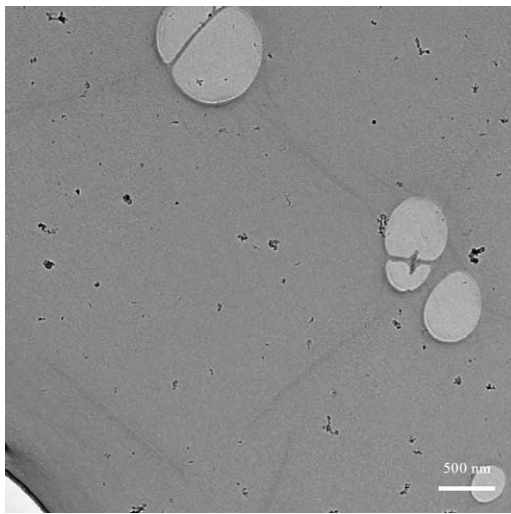
(b)

Fig. 6. TEM images before and after oxidation for a group of particles. (a) Size-classified soot particles before oxidation ($d_m = 50$ nm). (b) After oxidation (4 min at 450 °C of furnace set temperature).

(a)

(b)

Fig. 7. TEM images before and after oxidation for a group of particles after digital filtering to remove background. (a) Size-classified soot particles before oxidation ($d_m = 50$ nm). (b) After oxidation (4 min at 450 °C of furnace set temperature).

3.2. Projected area equivalent diameter vs mobility equivalent diameter

In order to quantify these results it is necessary to understand the relationship between projected area equivalent diameter (d_A) and mobility equivalent diameter (d_m). DMA selected particle mobility diameters (50, 100, 130, and 150 nm) and we obtained TEM samples for each selected size using the procedure illustrated in Fig. 1a. Both d_A and d_m are orientation-averaged properties, since the agglomerates are ex-

pected to rotate randomly in a DMA column and in an impactor. Figures 9a, 10, and 11 show size distributions of the TEM samples for a given mobility diameter as a function of d_A. Figure 9a shows that the selected mobility size from the DMA (50 nm) coincides with the peak of the projected area equivalent diameter obtained by analyzing the particles on the TEM grid. We also observe a second peak at 75 nm. The DMA selects particles of a specified mobility and while most particles are singly charged a smaller fraction will be doubly charged and will also exit the
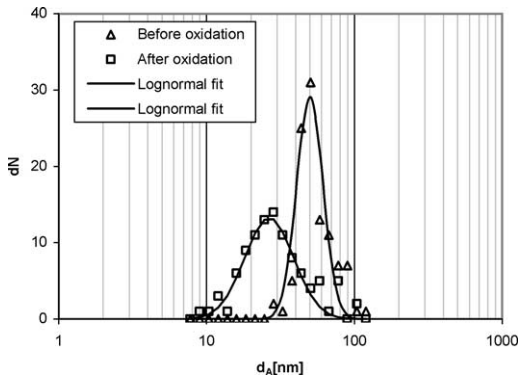
Fig. 8. Size distribution as a function of projected area equivalent diameter (d_A) before and after oxidation. Data for the lognormal fit were selected in a monotonic decreasing fashion from the peak for Figs. 8–14. Data that do not obey this monotonic decrease were excluded for the lognormal fit.

DMA. In this case, the second peak (at 75 nm) corresponds to particles of the same electrical mobility but with two charges.

This observation is not new. Wen and Kasper [15] observed a peak from doubly charged particles when they deposited size-selected chain agglomerates with a DMA on a TEM grid using a thermal precipitator. Rogak et al. [16] conducted a very thorough investigation by comparing d_A determined by TEM image analysis with d_m determined by a DMA. They observed that d_m and d_A were essentially equivalent for TiO_2 agglomerates of size less than 400 nm. Figure 9b shows a mobility size distribution measured using the tandem-DMA method [9] shown in Fig. 1c, with the furnace turned off. The peak, which is around 75 nm in d_m as shown in Fig. 9b, represents particles which were doubly charged when they passed through the DMA-1 but singly charged when they passed through the DMA-2 shown in Fig. 1c. The excellent agreement between Figs. 9a and 9b confirms that d_m is effectively equivalent to d_A in the size ranges of interest to this study. Naturally, the TEM data are noisier because we limited the analysis to only 100 particles, while the DMA effectively is sampling several orders of magnitude of particles. Figures 10 and 11 show examples of the number size distribution as a function of d_A for different DMA size selections ($d_m = 100$ and 150 nm). There was no obvious peak in the number size distribution found for multiply charged particles, but there are significant counts at the approximate place where a particle of equivalent mobility and doubly charged should appear (151 and 234 nm, respectively, for a 100- and 150-nm DMA selection). One likely explanation is that the peak in the number distribution of soot particles from the flame source is ∼100 nm. This means the number concentration of larger doubly charged
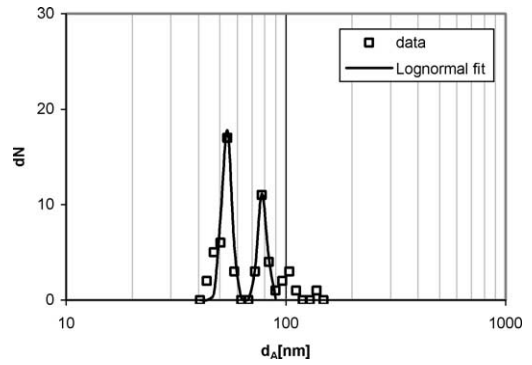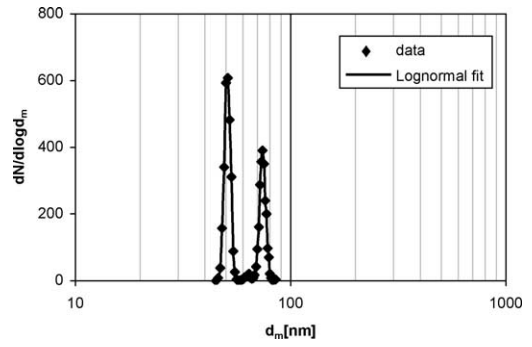
Fig. 9. Comparison between size distributions measured as a function of projected area equivalent diameter (d_A) and as a function of mobility equivalent diameter (d_m) for a given mobility diameter selection ($d_m = 50$ nm) by a DMA. (a) TEM measurement. (b) Tandem-DMA measurement.
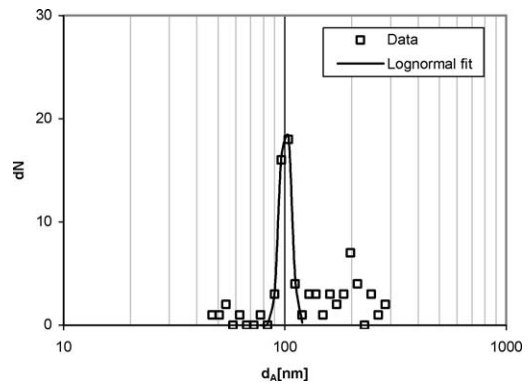
Fig. 10. Size distribution as a function of d_A when DMA selects $d_m = 100$ nm.

particles could be unnoticeable at a mobility size selection larger than 100 nm. Figures 12a–12c show TEM images at the same magnification for $d_m = 50$, 100, and 150 nm, respectively. Figure 13 shows that the relationship between d_m and d_A is linear, with a
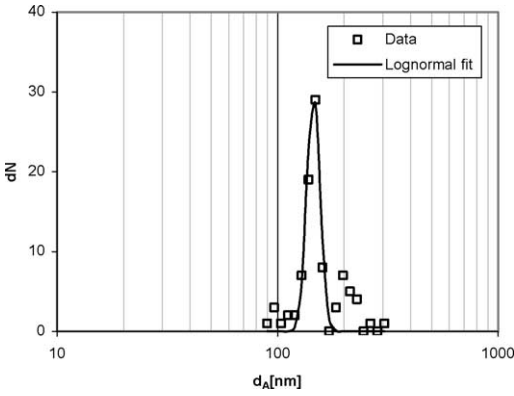
Fig. 11. Size distribution as a function of d_A when DMA selects $d_m = 150$ nm.

slope of unity for all measurements including those shown in Figs. 9a, 10, and 11.

3.3. Determination of the oxidation rate

The decrease in the mobility diameter of soot particles after undergoing oxidation was translated into an oxidation rate as in our previous work by Higgins et al. [9]. The oxidation rate of soot can also be obtained from the decrease in d_A by substituting d_m with d_A in Higgins et al.'s [9] Eq. (6), since we determined that d_A equals d_m.

We define the oxidation rate as

$$\frac{dm_s}{dt} = -\dot{w} A_s, \tag{1}$$

where m_s is the soot particle mass, $\dot{w}$ the surface specific rate, and A_s the soot surface area. The surface area for mass transfer of the soot particles in the free molecular regime is πd_m^2. By definition the effective density is

$$m_s = \rho_{\text{effective}} \frac{\pi d_m^3}{6}. \tag{2}$$

After mass and area are expressed in terms of the mobility equivalent diameter, Eq. (1) becomes

$$\frac{dd_m}{dt} = -\frac{2\dot{w}}{\rho_{\text{effective}}}. \tag{3}$$

Since this study does not measure the effective density, small-size agglomerates ($d_m = 50$ nm) were sampled for the oxidation experiment and assumed to be of constant density. This is equivalent to saying they are spherical. The density of soot was assumed to be 1800 kg/m^3, as suggested by Kennedy [17]. The mass-based surface specific oxidation rate, $\dot{w}$, is often modeled using a modified Arrhenius expression,

$$\dot{w} = A T^{1/2} \exp\left(\frac{-E_a}{RT}\right), \tag{4}$$
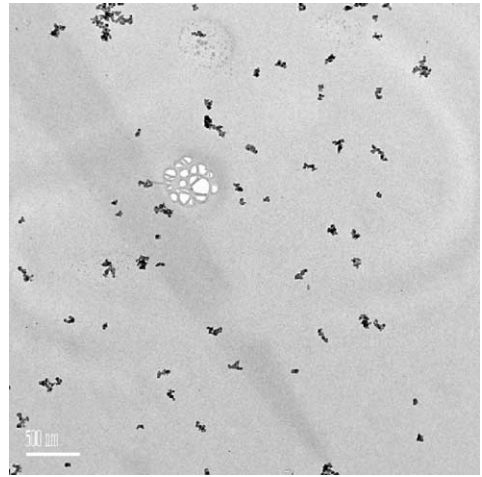
(a)
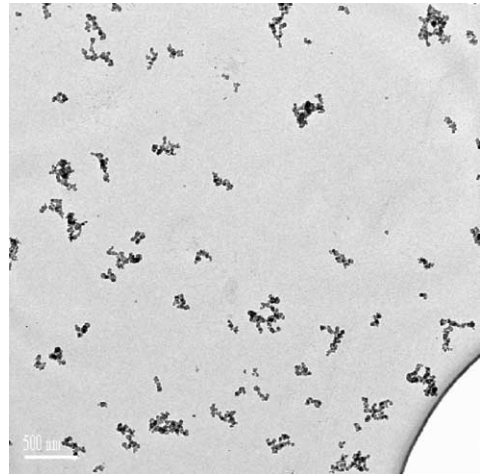
(b)
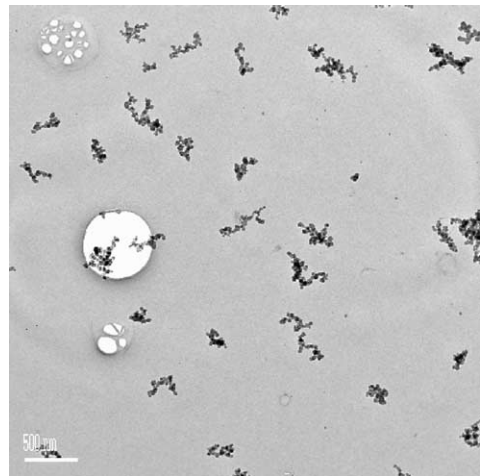
(c)

Fig. 12. TEM images at different d_m selections. (a) $d_m = 50$ nm, (b) $d_m = 100$ nm, (c) $d_m = 150$ nm.
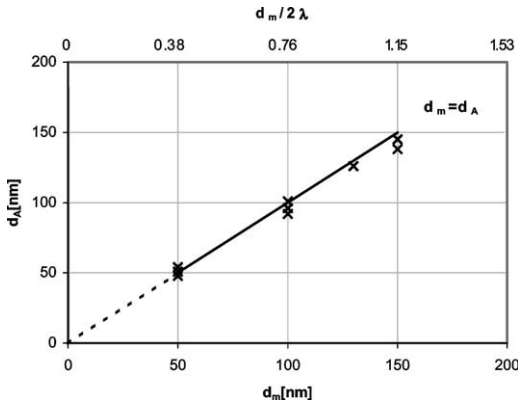
Fig. 13. The relationship between d_A and d_m for soot agglomerates. $d_m/2\lambda$ is the normalized particle diameter by 2λ, where λ is the mean free path of the carrier gas (here, it is air at room temperature).

where A is the preexponential factor, E_a is the activation energy, R is the gas constant, and T is temperature in Kelvin.

Since the given temperature was not constant with time as shown in Fig. 4, Eq. (3) is integrated over exposure time as follows:

$$\Delta d_m = \Delta d_A = \int_0^t -\frac{2\dot{w}(t)}{\rho}\, dt. \qquad (5)$$

Equation (5) gives the relationship between the surface specific oxidation rate and the change in projected area equivalent diameter. Given the experimental data of Δd_A at different furnace set temperatures, a least-square fit was carried out along with the integration shown in Eq. (5) to determine A and E_a for $\dot{w}$.

3.4. Comparison of rates with prior studies

In order to help in the validation of this work we have compared our results with our prior tandem-DMA measurements of Higgins et al. [18]. Unfortunately the oxidation experiment of Higgins et al. [18] could not be performed at the low temperature range used in this study, because of the long residence time needed. Instead the comparison was conducted at the higher temperature range. The comparison then was between an experiment done with configuration shown in Figs. 1b and 1c. The size distributions at 25 °C (room temperature) and a furnace temperature of 1000 °C were compared using DMA-2 and TEM image analysis and are presented in Fig. 14. The two experimental methods show excellent agreement in the most probable particle diameter before and after oxidation and are further proof that the project area equivalent diameter, d_A, is equivalent to the electrical mobility diameter, d_m.

(a)

(b)
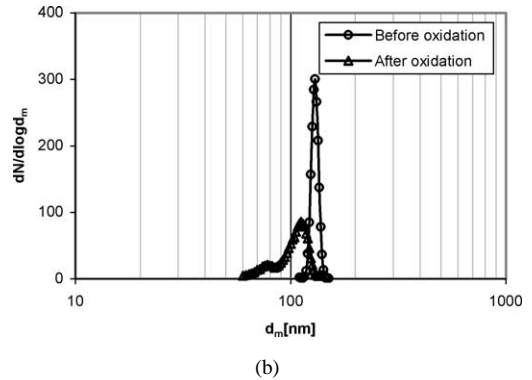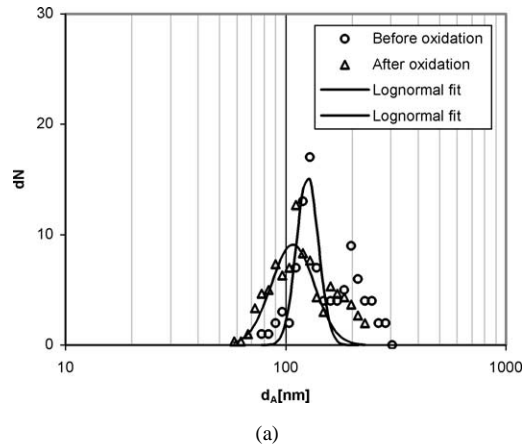
Fig. 14. Comparison of the results of Higgins et al. [18] with the current study. (a) TEM measurements before and after oxidation at 1000 °C. (b) Tandem-DMA measurement before and after oxidation at 1000 °C of furnace set temperature.

Figure 15 shows Arrhenius plots of the surface specific oxidation rate for our measurements and prior studies. The activation energy of low-temperature flame soot oxidation was determined to be 148 kJ/mol for low temperatures and is consistent with the 143 kJ/mol used in the Nagle and Strickland-Constable (NSC) [19] oxidation model (curve d in Fig. 15) as extracted by Stanmore et al. [20]. However, our oxidation rate is an order of magnitude higher than the extrapolated NSC model and even more than that for the other studies presented in this temperature range. To assess the possibility that this experimental approach somehow results in a higher observed reaction rate, we conducted an experiment under the same conditions (i.e., higher temperature) as in our prior tandem-DMA oxidation work [9,18]. Here the setup shown in Fig. 1b was used and the TEM was used to find size distributions before and after the furnace. The result is shown in Fig. 15 as the open circle, and overlaps with excellent agreement with rate curve c, of Higgins et al. [18]. This
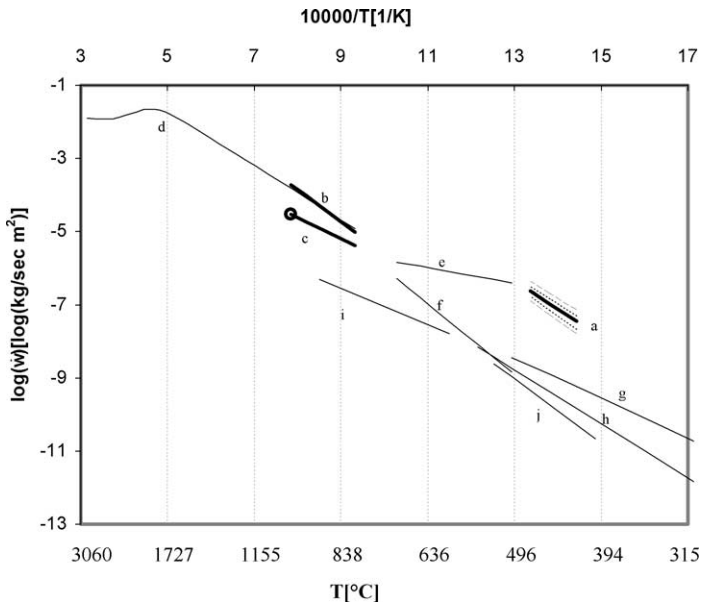
Fig. 15. Arrhenius plot of the surface specific rates of soot oxidation for the current study and for other relevant prior studies. Previous studies produced a variety of activation energies, as can be seen by the varying slopes of the lines. Results are presented for 21% O_2. (Curve a) Current study (—), rates for $\pm 1\sigma$ confidence lines (- - -), rates for ± 20 K variation (—). (Curve b) Higgins et al. [9] using flame-generated soot. (Curve c) Higgins et al. using diesel soot [18]. (Curve d) Nagle and Strickland-Constable [19] using a pyrographite rod. (Curve e) Miyamoto et al. [23] TGA of catalyzed (Ca added to fuel) diesel soot. (Curve f) Miyamoto et al. [23] TGA of uncatalyzed diesel soot. (Curve g) Ahlström and Odenbrand [3] flow reactor study of diesel soot. (Curve h) Otto et al. [1] TGA of diesel soot. (Curve i) Gilot et al. [2] TGA of carbon black. (Curve j) Neeft et al. [4] flow reactor study of Printex-U flame soot from Degussa AG.

would suggest that the TEM sizing approach should be yielding accurate results at the lower temperature conditions.

To assess other possibilities for our higher rate, the soot sampled on the TEM grid was pretreated under a N_2 environment at 550 °C for 5 min to rule out the possibility that volatile organics may be enhancing the apparent oxidation rate. The temperature and residence time for the pretreatment were taken from the IMPROVE method [21]. We observed no noticeable size change after N_2 pretreatment, nor was there any subsequent change in the observed oxidation rate.

Another possibility considered was that the soot which was in contact with the SiO_2 TEM grid might somehow accelerate oxidation; however, van Doorn et al. [22] have shown that SiO_2 has no catalytic effect on diesel soot particles. One may expect a lower activation energy along with an increased rate if catalytic effects are important as observed by Miyamoto et al. [23]. In their work they saw enhanced rates for calcium-laden diesel soot of up to 2 orders of magnitude higher (curve e in Fig. 15) compared with undoped soot (curve f in Fig. 15).

Temperature is one of the most sensitive variables in determining reaction rate. Our uncertainty analysis

discussed in Appendix A indicates an uncertainty of less than ± 2 K. If one were to assume a worst case scenario and assume an uncertainty 10 times larger, the resulting effect on the rate is shown in Fig. 15, as the thin lines above and below rate curve a. Obviously uncertainty in temperature cannot explain our observed higher rate.

The uncertainty related to the image analysis is also discussed in Appendix A. The uncertainty in the measurement of a 20-nm diameter is expected to be less than ± 2 nm. However, for particles below 20 nm, the uncertainty increases due to a decrease in the number of pixels which constitute a given particle. The dotted lines seen in Fig. 15, curve a, show $\pm 1\sigma$ confidence lines. The propagation of the uncertainty in determination of d_A to the final rate is negligible, since it lies within the confidence line limits above.

Stanmore et al. [20] in their recent review have discussed the variation in the measured oxidation rates, some of which are presented in Fig. 15. They suggested the possibility that some of the measured rates might be corrupted by mass transfer effects, which would tend to make the observed rate lower. We should also note that in the low temperature range, curve j reflects results for black carbon, while curves

h and g are diesel soot results from Otto et al. [1] and Ahlström and Odenbrand [3], respectively. This difference in source may also create differences in measured rates.

Ishiguro et al. [6] studied the microstructure evolution for diesel soot oxidation at about 800 K using an analytical electron microscope. During oxidation they observed flaking of crystallites from the outermost shell of the particles. This would certainly make the apparent rate higher than NSC prediction; however, that does not explain the discrepancy between our results and the other low-temperature data. Furthermore, given the resolution of our instruments we were not able to assess if this flaking phenomenon was taking place for our particles.

So at this point we are left without a firm conclusion as to why we observe these differences with prior results. Since the imaging method presented here gave results similar to those of our tandem-DMA studies under the same conditions, we conclude that our higher rate is attributable to a measurement protocol that more effectively assesses the intrinsic chemical reactivity, without the corruption of heat and mass transfer effects associated with bulk methods. These results are consistent with our single-particle mass-spectrometry studies on condensed-phase chemical kinetics, in which we observed much higher reaction rates for small particles over bulk samples [5].

4. Conclusion

An experimental protocol was developed to visualize oxidation of soot at low temperatures and to measure the oxidation rate of soot particles using TEM image analysis. The visualization of individual soot particles showed the disappearance of a portion of the soot aggregates during oxidation. A group of soot particles was tracked to better represent the changes in d_A during oxidation. TEM samples using an impactor after size classification by DMA gave number distribution as a function of projected area equivalent diameter, d_A, at given mobility diameter, d_m. The size distributions obtained from the TEM images confirm that d_m equals d_A as Rogak et al. [16] observed using TiO_2 agglomerates. The relationship between d_m and d_A was used to convert the change in projected area to the oxidation rate of soot particles after slightly modifying the conversion equation developed by Higgins et al. [9]. The surface area specific oxidation rate of soot particles at temperatures below 800 K was found higher than that found in prior studies. The rates determined using the TGA method may be lower due to limitations of heat and mass transfer that Mahadevan et al. [5] found in the bulk method. In conclusion, the experimental protocol developed

for this project can be used to measure reaction rates and to visualize the reaction at the same time for a variety of applications, overcoming the limitation of heat and mass transfer seen in the conventional thermal method. Further work is necessary to identify what caused the difference between low- and high-temperature oxidation rates.

Appendix A. Uncertainty and error analysis

A.1. Uncertainty related to temperature measurement

Temperature measurement is very important in determining reaction rates since temperature is one of the most sensitive variables. The gas temperature profile shown in Fig. 4 is based on temperature measurements taken on top of the TEM grid after the crucible was placed in the middle of the furnace as shown in Fig. 3. The K-type thermocouple, with a diameter of 0.05 mm (Model CHAL 001; Omega), was used and its response time is approximately 0.05 s due to its ultralow heat capacity. To confirm whether the temperature of a TEM grid follows the gas temperature, temperature readings were taken using the same type of thermocouple as that attached to the TEM grid. The increase in total heat capacity due to the attached TEM grid did not cause noticeable temperature delay, which implies that the TEM grid also has a negligible amount of heat capacity. The effect of radiation heat transfer was assessed by measuring steady-state temperatures using two types of thermocouple probes after 4 min of elapsed time. A radiation-shielded thermocouple probe (Omega) and an exposed-tip thermocouple probe (Omega) with a tip diameter of $1/16$ in. were used to measure the gas temperature after 4 min of elapsed time. These two probes have longer response times due to their high heat capacity. The above four measurements showed agreement within ± 1.5 K, after 4 min of elapsed time, and implies that radiation heat transfer effects could be ignored.

A.2. Uncertainty related to the TEM image analysis

Determining a threshold for digital filtering is the most important procedure for differentiating soot particles from background. In particular, images with
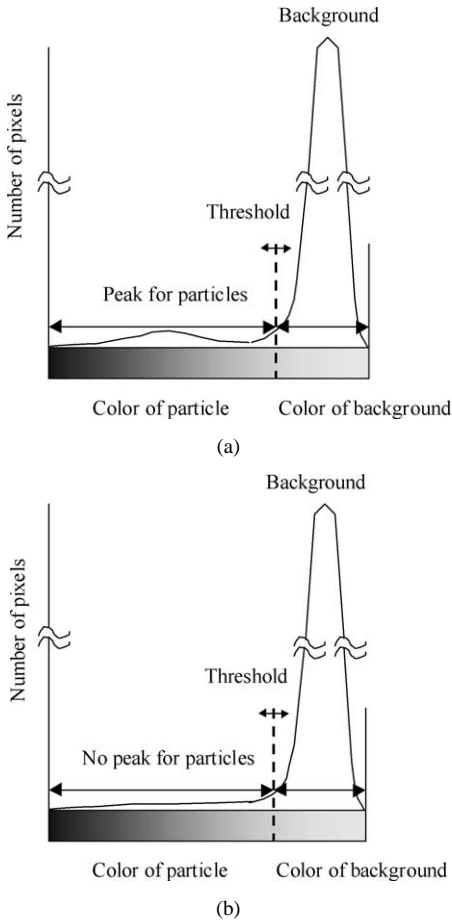
Fig. 16. Typical histograms of the TEM images. (a) Ideal case. (b) As observed (reproduced, by permission of the publisher, from [24]).

high contrast between particles and background are best for data analysis. Figure 16 shows histograms of pixel counts as a function of color brightness. Ideally, a histogram of an image containing particles will have two major peaks as shown in Fig. 16a: one for the background and the other for the particles. In practice, the peaks may not be clearly distinguishable as shown in Fig. 16b (Gatan, Inc. [24]).

Because each TEM image will have a slightly different contrast determination of the background, threshold level varies from image to image. It was necessary therefore to manually set the threshold for each image. Several images were taken for the same field of view to determine uncertainty in determining d_A. Each image was thresholded with five different settings and the average diameter and upper and lower limit diameters of a given particle were determined from each thresholding of all the images. The results of this analysis indicated an uncertainty

of less than 2 nm for a 20-nm-diameter primary particle.

References

[1] K. Otto, M.H. Sieg, M. Zinbo, L. Bartosiewicz, SAE Technol. Pap. 800336, 1980.
[2] P. Gilot, F. Bonnefoy, F. Marcuccilli, G. Prado, Combust. Flame 95 (1993) 87.
[3] A.F. Ahlström, C.U.I. Odenbrand, Carbon 3 (1989) 475.
[4] J.P.A. Neeft, T.X. Nijhuis, E. Smakman, M. Makkee, J.A. Moulijn, Fuel 76 (1997) 1129.
[5] R. Mahadevan, D. Lee, H. Sakurai, M.R. Zachariah, J. Phys. Chem. A 106 (2002) 11083–11092.
[6] T. Ishiguro, N. Suzuki, Y. Fujitani, H. Morimoto, Combust. Flame 85 (1991) 1.
[7] T. Tanaka, in: 22nd International Vienna Engine Symposium, vol. 2, OVK and Technical Univ. of Vienna, 2001.
[8] R.J. Santoro, H.G. Semerijan, R.A. Dobbins, Combust. Flame 51 (1983) 203.
[9] K.J. Higgins, H. Jung, D.B. Kittelson, J.T. Roberts, M.R. Zachariah, J. Phys. Chem. A 106 (2002) 96–103.
[10] S.V. Hering, S.K. Friedlander, J.J. Collins, L.W. Richard, Environ. Sci. Technol. 13 (1979) 184–188.
[11] F.A. Heckman, Rubber Chem. Technol. 37 (1964) 1245.
[12] P. Gilot, F. Marcuccilli, G. Prado, Corrosion of Advanced Ceramics, 1963, pp. 329–339.
[13] W. Hess, M.C.R. Herd, in: J.B. Donnet, R.C. Bansal, M.-J. Wang (Eds.), Carbon Black, second ed., Dekker, New York, 1993, chapter 3.
[14] NIH Image, Image software developed at the U.S. National Institutes of Health and available on the Internet at http://rsb.info.nih.gov/nih-image/.
[15] H.Y. Wen, G. Kasper, Aerosol Sci. Technol. 3 (1984) 397.
[16] S.N. Rogak, R.C. Flagan, H.V. Nguyen, Aerosol Sci. Technol. 18 (1993) 25.
[17] I.M. Kennedy, Prog. Energy Combust. Sci. 23 (1997) 95.
[18] K.J. Higgins, H. Jung, D.B. Kittelson, J.T. Roberts, M.R. Zachariah, Environ. Sci. Technol. 37 (2003) 1949–1954.
[19] J. Nagle, R.F. Strickland-Constable, in: Fifth Carbon Conference, vol. 1, Pergamon, Oxford, 1962, pp. 154–164.
[20] B.R. Stanmore, J.F. Brilhac, P. Gilot, Carbon 39 (2001) 2247–2268.
[21] J.C. Chow, J.G. Watson, D. Crow, D.H. Lowenthal, T. Merrifield, Aerosol Sci. Technol. 34 (2001) 23.
[22] J. van Doorn, J. Varloud, P. Mérıaudeau, V. Perrıchonı, Appl. Catal. B 1 (1992) 117.
[23] N. Miyamoto, H. Zhixin, O. Hideyuki, SAE Pap. 881224, 1988.
[24] Gatan, Inc., Digital Micrograph User's Manual v.3.3, 1998.